




**Living on the edge: Topology, electrostatics, and disorder**Tineke L. van den Berg <sup>1,2,\*</sup> M. Reyes Calvo <sup>3,4,5</sup> and Dario Bercioux <sup>2,4,†</sup><sup>1</sup>*Centro de Física de Materiales, 20018 Donostia–San Sebastián, Spain*<sup>2</sup>*Donostia International Physics Center, 20018 Donostia–San Sebastián, Spain*<sup>3</sup>*CIC nanoGUNE, 20018 Donostia–San Sebastián, Spain*<sup>4</sup>*IKERBASQUE, Basque Foundation for Science, 48013 Bilbao, Basque Country, Spain*<sup>5</sup>*Departamento de Física Aplicada, Universidad de Alicante, 03690 Alicante, Spain*

(Received 13 November 2019; accepted 14 January 2020; published 19 February 2020)

We address the coexistence of massless and massive topological edge states at the interface between two materials with different topological phases. We modify the well-known Bernevig-Hughes-Zhang model to introduce a smooth function describing the band inversion and the band bending due to electrostatic effects between the bulk of the quantum well and the vacuum. Within this minimal model we identify distinct parameter sets that can lead to the coexistence of the two types of edge states and that determine their number and characteristics. We propose several experimental setups that could demonstrate their presence in two-dimensional topological systems, as well as ways to regulate or tune the contribution of the massive edge states to the conductance of associated electronic devices. Our results suggest that such states may also be present in novel two-dimensional van der Waals topological materials.

DOI: [10.1103/PhysRevResearch.2.013171](https://doi.org/10.1103/PhysRevResearch.2.013171)**I. INTRODUCTION**

The study of edge states, or surface states for three-dimensional (3D) materials, goes back to the 1930s, when Tamm and Shockley studied bound states at the surface of a periodic lattice structure [1,2]. The discovery of the quantized transversal conductance in the integer quantum Hall effect (IQHE) in the early 1980s [3] revealed the existence of a new type of edge state. The measured quantized conductance is due to solely edge conduction, as it was realized only later [4,5]. Contrary to classical edge states, the conducting edge states in the IQHE result from properties of the bulk of the system, namely, its Landau levels; it turned out this was one of the first example of topological edge states [6]. Not only are these states robust to disorder, but it is even desirable to invoke disorder for understanding why it is relatively easy to measure the conductance plateaus. Moreover, to capture the details of the spatial distribution and interactions between edge states, a proper description of the electrostatic potential at the edge is needed [7,8].

It was thought for a long time that one necessarily needed the breaking of time-reversal symmetry (TRS) in order to get quantized conduction at the sample edges. With the theoretical discovery of the topological insulator (TI), it was realized that different symmetry classes could also give rise to systems

with edge conduction in the absence of an external magnetic field (for reviews see [9–12]). The first type of nontrivial system that was proposed was one giving rise to the quantum spin Hall effect (QSHE) [13,14]. In particular, this effect was predicted to be present in 2D mercury telluride quantum wells (QWs) grown on cadmium telluride substrates (HgTe/CdTe) [15] (for a recent review see Ref. [16]). Band-gap inversion in the bulk gives rise to two spin-locked counterpropagating modes at the edges with linear dispersion (massless). These edge modes are protected from disorder by TRS, and the  $2e^2/h$  two-terminal conductance plateau extends throughout the entire gap. Here no electrostatics are invoked to understand their spatial distribution at the edge. The expected  $2e^2/h$  quantized conductance was indeed measured about a year after the proposal [17]. Quantum wells of HgTe/CdTe became one of the standard platforms for investigating the QSHE in 2D systems; nonlocal dissipationless transport has been measured [18], the helicity of the edge channels was demonstrated [19], the edge currents were visualized [20,21], and the interactions between edge states were recently probed [22,23]. Besides in 2D HgTe QWs, experimental signatures of edge states in the QSH regime have also been predicted and observed in other platforms such as GaAs/InSb QWs [24–27] and in monolayer  $1T'$  phases of transition metal dichalcogenide crystals of  $WTe_2$  and  $WSe_2$  [28–31], bismuthene [32–34], and other layered materials [35].

Still, observation of conductance quantization in the QSHE is never as precise as is observed in the IQHE, and even in small and clean samples conductance is always fluctuating substantially, up to 10% or 20% of  $2e^2/h$ . Besides being due to residual bulk or surface conduction, several other mechanisms have been proposed to explain the origin of these fluctuations [36–42]. The most important source of fluctuations is thought to be disorder, or to be specific, disordered charge

\*tineke.vandenberg@dipc.org

†dario.bercioux@dipc.org

puddles in topological quantum wells, for example, HgTe/CdTe. Although QSH edge states are in principle protected from disorder, disordered charge puddles can be a possible source of decoherence. The electrons, while wandering around in the puddle, may undergo inelastic scattering, losing coherence and potentially scattering back into a reverse-direction edge state, which would result in lower than  $2e^2/h$  edge conduction [40–42]. In the following, we will focus on a mechanism that can induce fluctuations above  $2e^2/h$ , namely, the coexistence of additional edge states. Such Shockley-type edge states can arise from electrostatic interface effects, such as band pinning or band bending, and the presence or absence of a topological edge state is not a requirement. In contrast to the linearly dispersive (massless) topological states, such states have a parabolic-like dispersion relation and so are said to be massive edge (ME) states. Besides electrostatic boundary effects, another possible origin of ME states at topological interfaces, discovered by Volkov and Pankratov [43], is the smooth (instead of abrupt) band inversion at the edge. States resulting from this effect are called Volkov-Pankratov (VP) states in the literature, and these states are of topological origin, in the sense that they are the result of the lifting of band inversion between a topological and a trivial material. These VP states always accompany a massless topologically protected state, although in the original paper by Volkov and Pankratov the proposed band inversion was associated with a gradient in the doping percentage of IV–VI semiconductors [44]. Recently, VP states have attracted attention again, when they were observed to reside in 3D strained HgTe systems [45–47].

Here we investigate the presence of ME states of topological and/or electrostatic origin, in 2D topological systems, within the Bernevig-Hughes-Zhang (BHZ) toy model. Within this model, we implement smooth band inversion and electrostatic edge effects, in order to investigate the behavior of ME states in a generic setting. We also add disorder to the model, thereby demonstrating the different response to disorder of unprotected and topologically protected edge states. We propose four experiments that could detect ME states and strategies for tuning their contributions to conductance. Those contributions could be tuned off, if undesired when only clean topological transport is aimed for, or used for selective switching in multivalued logic devices [48].

In Sec. II we will discuss the case of edge states due to electrostatics in normal systems and how the situation changes in topologically nontrivial systems. In Sec. III we will start by introducing the BHZ model (Sec. III A) and then discuss how we adapt the model in order to include interface effects (Sec. III B). We will study the spectral properties, both charge and spin degrees of freedom (Sec. III C). We will then add disorder to the model, before continuing to investigate the transport properties (Sec. III D). In Sec. IV we will propose four different experimental setups for detecting massive edge states in 2D devices. We summarize in Sec. V.

## II. ELECTROSTATICS NEAR DEVICE EDGES

The fact that many semiconductors have low densities of free carriers results in long space-charge regions. This again leads to bending of the band structure at the interface,

particularly when an electric field is applied to the system by means of a gate electrode in a field-effect transistor geometry, in which case pinning of the Fermi level at the interface can substantially enhance the bending. Depending on the sign and magnitude of the band bending, the interface layer is classified as a depletion, accumulation, or inversion layer [49]. If one would like to know the precise spatial variation of the bands at the interface of a specific material, one should solve the Poisson equation, together with the Schrödinger equation if quantum effects are important, which is generally the case for strong band bending. These two equations should be solved self-consistently, taking into account the specific details of the material and imposing overall charge neutrality. Without going into such detail, we can take a look at a very general simple case. If one wants to know the precise spatial variation  $V(y)$  of the band bending near the interface, one must solve Poisson's equation

$$\frac{d^2V(y)}{dy^2} = -\frac{\rho(y)}{\epsilon_0\epsilon_m}, \quad (1)$$

where  $\rho(y)$  is the density of the charge per unit area (or unit volume in three dimensions) and  $\epsilon_{m(0)}$  is the dielectric constant of the material (vacuum). Because the band structure does not remain flat near the interface, a quantum-well-like potential landscapes appears, creating room for states close to the interface. These edge states carry a certain charge, which is equilibrated behind the interface over a certain distance, usually called the interface length. For moderately strong bending such that quantum effects can be neglected, this slab of material at the interface is called the depletion layer, and one can affirm that the density of the charge is approximately constant in space, i.e., assuming  $\rho(y) \propto eN_D$ , where  $N_D$  is the density of the charges. These assumptions result in a band bending that is quadratic in space

$$V(y) = -\frac{eN_D}{\epsilon_0\epsilon_m}(y - y_{\text{int}})^2, \quad (2)$$

where  $y_{\text{int}}$  is the interface length over which the bending occurs. This length scale depends on the dopant density of the material and on how strong the bending is. For strong enough bending, and depending on whether the bending is up or down, edge states might appear either below the conduction band (CB) or above the valence band (VB) [49].

The solution to Poisson's equation at interfaces is known for many different settings, with more or less intricate solutions. However, in topological insulators there is another ingredient, which is the presence of a metallic state near the interface, namely, the topological edge state. This topological metallic edge state will introduce different screening effects, likely more pronounced once a gate potential is applied to the system. In order to calculate the exact spatial electron density, one has to solve the Poisson equation and the Schrödinger equation self-consistently, given all of the systems ingredients. This is an arduous task, moreover, because in many realistic systems the charge neutrality point of this state can be buried in the valence band [50]. Doing this calculation, for example, for HgTe or InAs/GaSb QWs, goes beyond the scope of this work. However, in order to study the general physical aspects of ME states, it turns out the exact details

of the interface function are of minor importance, as long as some general features are correctly taken into account [46].

### III. EDGE STATES IN THE TOPOLOGICAL BHZ MODEL

The QSHE in HgTe/CdTe and InAs/GaSb QW systems is usually addressed within an eight-band  $\mathbf{k} \cdot \mathbf{p}$  model [14,24]. It was shown that for a layer of HgTe larger than a critical thickness, the QW undergoes a topological phase transition resulting in spin-locked in-gap edge states [15]. A similarly topological phase transition was predicted in the InAs/GaSb QW system induced by the effect of an electrostatic gate [24]. In addressing transport properties, however, this  $\mathbf{k} \cdot \mathbf{p}$  model is not very convenient because it demands substantial numerical resources. The BHZ model is a reduction of the  $\mathbf{k} \cdot \mathbf{p}$  theory which contains only the four bands closest to the Fermi energy while keeping the most important physical aspects. This model is both accurate and convenient for studying in-gap spectral and transport properties. It can be studied in the trivial regime or in the topological regime, depending on the sign of the gap parameter [15,51]. In the following, we summarize the main properties of the BHZ model. We then present a modification of it that allows for investigating the consequences of interface effects, namely, the emergence of ME states.

#### A. Bare BHZ model

The standard four-band BHZ model in spin and band subspace reads

$$\mathcal{H} = \begin{pmatrix} h(\mathbf{k}) & 0 \\ 0 & h^*(-\mathbf{k}) \end{pmatrix}, \quad (3)$$

with the spin-subblock Hamiltonians

$$h(\mathbf{k}) = \begin{pmatrix} (M + C) - (B + D)\mathbf{k}^2 & Ak_+ \\ Ak_- & (C - M) + (B + D)\mathbf{k}^2 \end{pmatrix}, \quad (4)$$

where  $A, B, C, D$ , and  $M$  are material-dependent parameters,  $\mathbf{k} = \sqrt{k_x^2 + k_y^2}$ , and  $k_{\pm} = k_x \pm ik_y$ . The Hamiltonian in (3) is expressed in the basis

$$\{|e\uparrow\rangle, |h\uparrow\rangle, |e\downarrow\rangle, |h\downarrow\rangle\},$$

where  $e$  refers to electrons in the CB and  $h$  the VB and  $\uparrow$  and  $\downarrow$  are the spin eigenstates along the  $z$  direction. This model gives rise to a topologically nontrivial system when the following condition is fulfilled:  $0 < M/2B < 2$  [51]. The numerical results presented in the main text are obtained via the following set of parameters typical for HgTe/CdTe QWs:  $A = 0.3654$  nm eV,  $B = -0.686$  nm<sup>2</sup> eV,  $D = -0.512$  nm<sup>2</sup> eV, and a gap parameter in the topological regime of  $M = -10$  meV, which is half the gap width. This parameter set gives rise to a band structure like that depicted in Fig. 2(a). The gap is 20 meV ( $=2|M|$ ), as ideally expected in HgTe QWs at zero temperature. In the gap, between the conduction and the valence bands, lie two topological modes with a linear dispersion. The crossing point lies just under the conduction band. In most HgTe structures, one would expect a flatter valence band around the  $\Gamma$  point, with a camelback shape, and

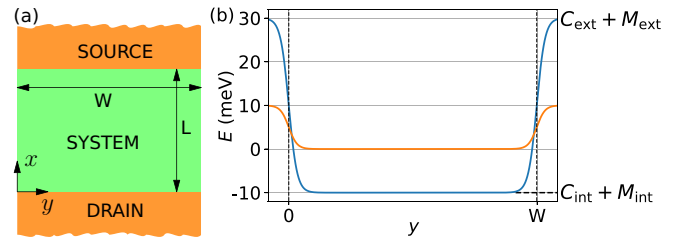


FIG. 1. (a) Sketch of the system and (b) lateral structure of the Fermi energy (orange line) and energy band onset (blue line) with band bending for  $k = 0$ . We used here the following parameters:  $C_{\text{int}} = C_{\text{ext}} = 10$  meV,  $M_{\text{int}} = -10$  meV, and  $M_{\text{ext}} = 20$  meV.

we should underline again that the BHZ model is constructed for reflecting the in-gap properties of 2D materials [15,50,52] and therefore should not be used to study the bulk properties of a system. However, as we are interested here in studying the in-gap (edge) properties, the BHZ model provides a good framework. A natural length scale that emerges from this model is  $\xi = \hbar v_F / |M|$ , where  $v_F$  is the Fermi velocity. In HgTe/CdTe QWs, with a bulk Fermi velocity of  $v_F = 5 \times 10^5$  m s<sup>-1</sup> and  $M = -0.01$  eV, this gives  $\xi = 200$  nm. We will later use this length scale when deciding on the interface length of our system.

#### B. Extended BHZ model: Interface effects

We will modify the bare BHZ model in order to make the band inversion and the electrostatic edge potential smooth and progressive. Therefore, in what follows, the parameters  $C$  and  $M$  will be functions of the lateral position  $y$  [see Fig. 1(b)]. Here  $M(y)$  will account for the smooth inversion of the topological gap and  $C(y)$  will account for band bending near the device edges. We will include these effects by writing the Fermi energy and the gap parameter of the system as a function of the form

$$F(y) = \frac{F_{\text{int}} + F_{\text{ext}}}{2} + \frac{F_{\text{int}} - F_{\text{ext}}}{2} \left[ \tanh\left(\frac{y}{\ell}\right) - \tanh\left(\frac{y-W}{\ell}\right) - 1 \right], \quad (5)$$

where  $F_{\text{int (ext)}} = M_{\text{int (ext)}} (C_{\text{int (ext)}}$ ) is the gap parameter (Fermi level) inside (outside) the system and  $\ell$  is the interface length. The choice of the form of this function appears natural, fulfills all basic requirements, and corresponds to a regular choice taken in the literature [46,49]. We will not justify it by means of self-consistent calculations of the electrostatic landscape near the edge, which would be an extensive investigation by itself. However, changing this transition function to a different smooth function, such as  $F(y/\ell) \propto (y/\ell)^2$  or  $F(y) \propto \tanh[(y/\ell)^2]$ , does not qualitatively change the results, which gives this choice a solid basis for this study.

In Ref. [46] Tchoumakov *et al.* analytically solved a similar model for a 3D TI with these types of boundary conditions. However, because the BHZ model is quadratic in momentum it cannot be solved analytically with the same technique, and we therefore implemented it numerically using KWANT [53].

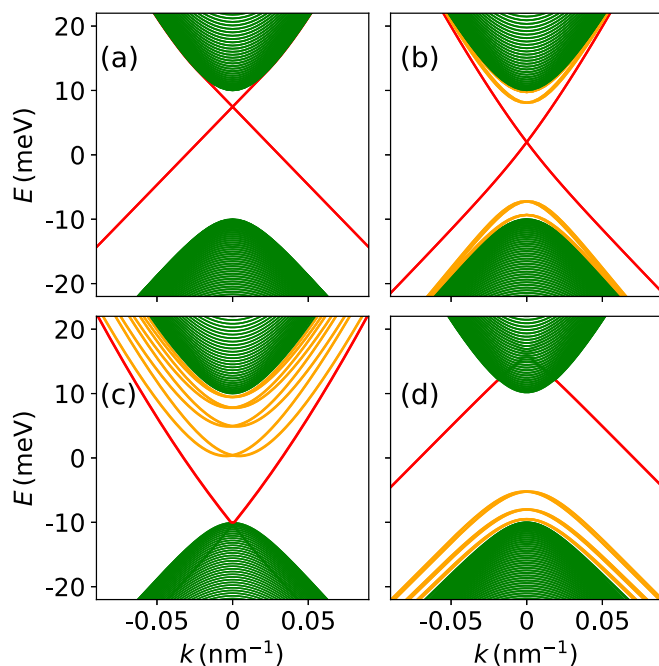


FIG. 2. Bulk bands (green), VP states (yellow), and topological edge states (red). The bare BHZ model is shown for HgTe parameters, with (a)  $C(y) = C = 0$  and  $M(y) = M = -10$  meV and (b) smooth band inversion with  $M_{\text{int}} = -10$  meV and  $M_{\text{ext}} = 10$  meV with the interface length  $\ell = 200$  nm and  $C(y) = 0$ . Also shown is sharp band inversion  $M(y) = M = -10$  meV, as in the bare model, and Fermi pinning near the edges with  $\ell = 200$  nm and (c)  $C_{\text{int}} = -20$  meV and  $C_{\text{ext}} = 20$  meV and (d)  $C_{\text{int}} = 10$  meV and  $C_{\text{ext}} = -10$  meV.

### C. Spectral properties

In order to obtain ME states in addition to the topological ones, one can change from an abrupt band inversion to a smooth band inversion, by taking  $M_{\text{int}} = -10$  meV and  $M_{\text{ext}} = 10$  meV and choosing an adequate interface length, which is done by taking  $\ell \gtrsim \xi$  in order to have a smooth gap inversion. The longer the interface length is, the more ME states can be hosted near the interface. We here choose  $\ell = 200$  nm, for which we get multiple well-detached ME states, which emerge both above the VB and under the CB [see Fig. 2(b)]. In this situation the ME states are also called Volkov-Pankratov states; they are of topological origin and always appear accompanying a topological state.

Another strategy for obtaining states at the edge is applying a local potential near the edge, which would physically correspond to a band bending scenario. By adding a local edge potential to the outermost lattice sites in the BHZ system, the crossing point of the topological states can be moved up or down, as was already shown in Ref. [50], and edge states may appear for strong enough potentials. Here we implement a physically more natural boundary potential given in Eq. (5), which has the same effect of moving the crossing point down (or up). This results in band structures as depicted in Figs. 2(c) and 2(d) if the sign of the potential is, respectively, negative or positive. In Fig. 2(c) the bending of the Fermi energy is positive, bending towards the conduction

band, and conversely, in Fig. 2(d), the Fermi energy bends towards the valence band. So depending on the sign of the bending, the ME states can hang under the CB [Fig. 2(c)] or lie above the VB [Fig. 2(d)]. Similar results were also obtained for the case of 3D TI [46]. The band structure at the edge forms a sort of triangular confinement potential at the boundaries of the system; the ME states can be seen as states arising from this confinement, each of them presenting a spin-split spectrum due to spin-orbit interactions, much the same as what was predicted for quantum wires with spin-orbit interaction [54–57].

For topological QWs exceeding a specific thickness,  $\mathbf{k} \cdot \mathbf{p}$  calculations hint at a burying of the crossing point of the topological mode inside the camelback of the valence band [50,52]. Within the BHZ model this configuration is recovered in the case of Fig. 2(c), and we will from now concentrate on this sort of configuration. The bending of the bands in this way, here implemented as a smooth on-site potential at the edge, not only accounts for finite-size effects, but can also reproduce interface electrostatic effects, inhomogeneous gating, electrostatic screening due to the existence of topological metallic states, or any other interface effects resulting in a smooth modulation of the bands towards the edge. Independently of where it may come from, it is used here to obtain the physical situation of interest. In addition to the band structure, we can analyze the local density of state (LDOS), which we will refer to as  $\rho(x, y)$ . In KWANT the LDOS is calculated for an open system, a scattering region connected to source and drain leads. The states in the scattering region, which is characterized by its scattering matrix, are the result of incoming modes at a given energy, from a given lead. In a clean system  $\rho$  is translationally invariant along the transport direction [and so has only a lateral variation  $\rho(y)$ ] and it is sufficient to study line cuts, as in Fig. 3(b). Here we have summed over all modes, coming in from the top (source) lead, at energies specified in the band structure of Fig. 3(a). This reveals that the massive states observed in yellow in the band structure of Fig. 3(a) only have a nonzero weight near the edges. It also tells us that the topological states exist closest to the edges and the consecutive ME states spread out away from the edge. This spatial distribution of the LDOS should be observable in local probe experiments, such as scanning tunneling spectroscopy (STS) or scanning gate microscopy (SGM) experiments (cf. Secs. IV A and IV B). Furthermore, the ME states present an oscillating behavior along the  $y$  direction that is not observed for the topological one. The origin of the oscillations in the LDOS can be found in the interference of modes at a fixed energy  $\mathcal{E}$ ; these are characterized by different values of the longitudinal momentum  $k_x^i(\mathcal{E})$ . We can express the LDOS of each mode of the system as

$$\rho(y, \mathcal{E}) = \sum_m \left| \sum_i \psi_m[y, k_x^i(\mathcal{E})] \right|^2, \quad (6)$$

where  $m$  is the associated mode index and we sum up over all the modes with energies smaller than or equal to  $\mathcal{E}$ . Modes with a higher energy  $\mathcal{E}$  oscillate more because they penetrate further into the bulk region of the QW.

Using the same method as for the LDOS, we can calculate the spin polarization. As known from the QSHE, the electrons

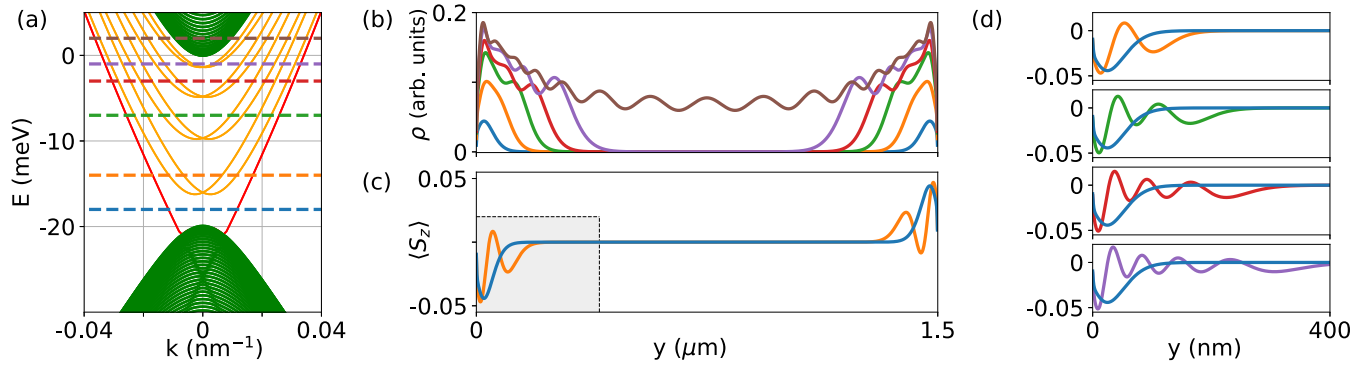


FIG. 3. (a) Band structure with smooth band inversion and band pinning, together with (b) the corresponding local density of states at energies as indicated in the band structure. The blue line shows the LDOS when the system contains only the topological edge states, one on each edge. For the orange, green, red, and purple lines, one spin-split and doubly degenerate edge mode is added each time, hosting two edge states at each edge. The brown LDOS line is in the conduction band, giving rise to bulk states. (c) The  $z$ -spin-resolved local density of states for the topological state (blue) and the first ME modes (orange). The gray area is shown in (d), containing the topological mode and consecutively adding the four ME states, as shown in the band structure of (a). For more details, see the Appendix.

in the topological conduction channels are spin- $z$  polarized [see Fig. 3(b), blue line]. The polarization is of opposite sign on opposite edges (upper part of the panel), as expected. The massive edge states also show polarization with respect to spin  $z$ , which is asymmetric on opposite edges; similarly to the LDOS, the behavior is oscillatory. For a system containing the topological state and one massive state on each edge (orange curves) there are two positive oscillations, for a system containing two massive states at the edge (green lines) there are three positive oscillations, etc. The expectation values of the spin- $x$  and spin- $y$  components are zero, as expected. There is, in the BHZ model, no Rashba or Dresselhaus type of spin-orbit interaction, because the model does not include any structural inversion asymmetry. If one were to add structural inversion asymmetry, one would shift the crossing point away from the  $\Gamma$  point, moving it to finite momentum values. The trivial edge states would also be shifted, but would otherwise stay unaffected. Due to the Rashba spin-orbit coupling, the massless and massive edge states would acquire a nonzero spin component along the  $y$  direction. Spin-orbit interaction effects in a BHZ-type model were discussed in detail in Ref. [58].

However, one has to take into account the fact that realistic samples always contain some amount of disorder, and this might blur the effect somewhat, especially if one has to deal with charge puddles [16]. However, as we will show in Sec. IV A, even in the presence of disorder, in STS measurements one should still observe clear signatures of ME states.

#### D. Transport properties

As we mentioned before, the BHZ model is especially suited for doing transport calculations. We will start here with a device with a geometry such as depicted in Fig. 1(a), i.e., a scattering region connected to a source and a drain lead. The parameters used in this section are the same as in the preceding section, thus giving us the band structure of Fig. 3(a). By tuning the position of the Fermi level, simulating what is done experimentally by applying an overall back-gate potential, one can scan through the entire band structure, thereby changing

the number of ME bands crossing the Fermi energy and thus contributing to transport. For the system under investigation this means that moving the Fermi level from the VB through the gap and into the CB, we successively add ME states, thus stepwise increasing the conductance.

Despite the fact that the additional edge states are not topologically protected, one can expect to observe their presence in transport measurements. If present, the two-terminal conductance in the gap will exceed  $2e^2/h$  for clean (or short) enough devices [see Fig. 4(b)]. In the case of a defect-free sample, transport of ME states is ballistic and one observes a step each time the Fermi level crosses the energy onset of a ME state. Starting just above the VB with a  $2e^2/h$  conductance, one would add  $4e^2/h$  at each opening of a ME state, as the two spin-split bands are doubly degenerate and run on each edge of the sample.

In a more realistic scenario the presence of disorder will substantially decrease the contribution of ME states to device conductance. We implement Anderson-type disorder, which means we take random on-site energies within an energy range  $[-U_0/2, U_0/2]$ . How much the contribution of the ME states decreases depends on both the device channel length and the disorder strength. Results for  $500 \times 1000 \text{ nm}^2$  systems are shown in Fig. 4(b). In the weak-disorder limit one should still observe steps in the conductance curve as one sweeps the Fermi level, such as for  $U_0 = 50 - 100 \text{ meV}$ . For systems with strong disorder or for sufficiently long channels, the conductivity decreases to  $2e^2/h$  in the gap, meaning the only conducting state left in the system is the topologically protected one. Here we have considered a wide enough sample and uncorrelated disorder so that percolation from one edge to the other across the bulk does not occur, even for strong disorder. Therefore, in our model, conduction cannot decrease below  $2e^2/h$ . In narrow devices, strong Anderson disorder can decrease the conductance below  $2e^2/h$ , due to percolation between the two opposite conducting edges via favorable energy paths [59]. If one were to implement correlated disorder, charge puddles could form. Then the conductance could decrease below  $2e^2/h$  due to percolation between the lateral edges via charge puddles throughout the entire device or due

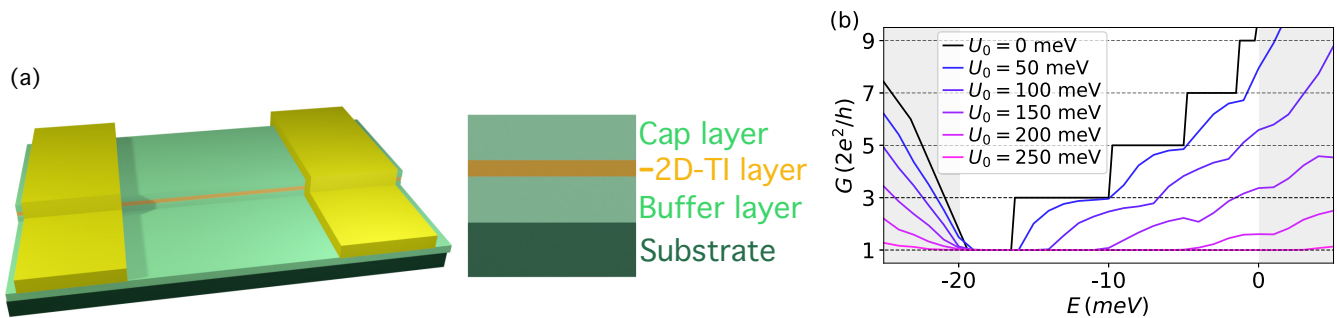


FIG. 4. Conductance as a function of Fermi energy for  $500 \times 1000 \text{ nm}^2$  systems, for a material with the band structure of Fig. 3(a). The black curve is for a clean system (no disorder) and the lines in purple are for successively stronger disorder, averaged over 80 disorder configurations.

to trapping of particles in the puddles resulting in inelastic scattering.

In Fig. 4(b) we observe a shifting of the energy of the conduction band opening as we increase the disorder strength. This is associated with a renormalization of the gap parameter and the Fermi energy due to the presence of the disorder, which was extensively discussed in Refs. [59–61] in the context of the topological Anderson insulator. The renormalization of the gap parameter  $M_{\text{int}} \rightarrow M_{\text{int}} + \delta M$  in the case of Anderson on-site energy disorder proportional to  $\sigma_0$  is negative  $\delta M < 0$ , thereby increasing the effective inverted band gap.

While hints of the existence of ME states can be extracted from transport measurements, we discuss in the next section other experimental approaches that could provide a more direct observation and characterization of the properties of ME states. On the one hand, STS spatial maps directly address the distribution of the system LDOS and can also be used to obtain the dispersion relations of the states through quasiparticle scattering, as shown in Sec. IV A. On the other hand, by exploring the effect of a movable local gate in the transport measurements, we can distinguish between conduction from bulk or edge states by using a so-called SGM, as shown in Sec. IV B.

#### IV. PROPOSALS FOR EXPERIMENTAL DETECTION AND TUNING

##### A. Local density of states mapped by scanning tunneling spectroscopy

In the analysis of the local density of states in Sec. III C, we have seen that it is possible to have several ME states in the system. The exact number will depend on the details of the system, namely, on how strong the band bending is and how long the interface length is. The number of ME states that will be filled depends on the position of the Fermi energy. Experimentally, this can be set by the potential applied to an overall back-gate electrode.

Assuming only elastic tunneling of electrons between the tip and sample, STS allows one to directly map the LDOS of a sample. The applied bias voltage between the tip and sample  $V_{\text{bias}}$  determines the energy of electrons injected into the sample  $eV_{\text{bias}}$  and the measured differential tunneling conductance at a given value of  $V_{\text{bias}}$  is directly proportional

to the LDOS at  $E_F + eV_{\text{bias}}$  [62]. Hence maps of differential conductance taken at a given  $V_{\text{bias}}$  are effectively spatial maps of the LDOS, at a given energy  $E_F + eV_{\text{bias}}$ . One could also address the LDOS at different energies by mapping the LDOS at near-zero  $V_{\text{bias}}$  and use a back-gate potential  $V_{\text{BG}}$  to tune the Fermi energy through the gap, producing maps at energies  $E_F(V_{\text{BG}})$ .

In the example of certain HgTe QWs as in Fig. 3(a), moving from the VB, through the gap, and into the CB increases the number of ME states contributing to the LDOS. Those states spread out away from the edge as more and more are added. In order to demonstrate the presence of additional dispersive modes in a 2D TI, one can therefore monitor the changes of the spatial distribution of the LDOS as a function of energy via STS maps. A prerequisite for observing the ME states in transport experiments is that the system is not too dirty, as disorder will eventually localize the unprotected edge states. However, as can be seen in Fig. 5, even in the presence of disorder the widening of the edge areas when increasing the number of available ME states can clearly be observed in the LDOS maps.

In Fig. 5 we note that the topological state is homogeneous in the  $x$  direction, even in the presence of disorder. In contrast, the ME states display standing-wave-type interference patterns, for which the period depends on the energy at which the LDOS is probed. Measuring the relation between the energy and the interference period, one can extract the dispersion relation of the one quasi-1D edge state (for a related example in another quasi-1D system, see Refs. [63,64]). A parabolic dispersion relation from quantum interference measurements would be a smoking gun for the existence of ME states. Quantum interference experiments have been used to probe the electronic structure of other topological systems [65]. At low energies, e.g., in Figs. 3(b)–3(d), the interference patterns are typical for quasi-1D modes, whereas Fig. 3(e) shows more typical interference patterns for a two-dimensional electron gas (2DEG) with impurities, as the highest ME state penetrates substantially into the bulk.

However, performing scanning tunneling microscopy experiments in buried structures is a rather challenging task. This phenomenology could be more easily explored in exposed 2DEG systems with an inverted band structure, such as bismuthene [32–34], the single layers of the  $1T'$  of some transition-metal dichalcogenides [30,31], or other layered

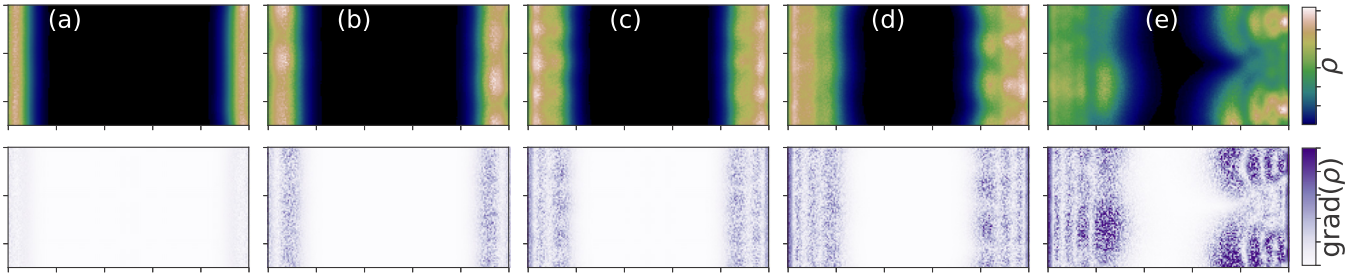


FIG. 5. Local density of states within the gap for a system with disorder with  $U_0 = 20$  meV (upper panels), starting with only the topological state (left) and including ME states successively, at energies corresponding to the lines in Fig. 3(a). The gradient of the LDOS (lower panels), which can be calculated after measurement of the LDOS, reveals the pattern of the wave functions, as well as interference effects due to scattering on impurities.

materials [35]. However, the necessary resolution in energy might be limited by the small size of the inverted gap, finite-temperature effects, and substrate interactions, which are yet more important for single-layer materials.

### B. Conductance measurements with scanning gate perturbation

Scanning gate microscopy is a technique especially suited to spatially mapping scattering in quasi-one-dimensional systems. In a SGM experiment we monitor the reaction of the system conductance to the perturbation induced by a local gate probe. The scanning gate is maneuvered above the sample and a positive or negative voltage is applied to the tip, experienced by the system as a locally applied electric field of positive or negative sign. The tip is typically held rather far away from the sample, some 10–100 nm. Due to this distance and to the conical shape of the tip, this typically results in a rather large region of the sample being subject to the tails of the electric field distribution. The spatial resolution therefore depends on the intensity of the response of the conductance of the system to small changes on electric field.

In the setup we propose here, by perturbing the system with the tip, one locally shifts the energy level that the sample area has within the band structure. Locally applying a negative electric field acts as placing a local barrier in the system, by lowering the energy of the electrons under the influence of the tip. On the other hand, a positive tip voltage will locally increase the energy of the underlying electrons. If we assume that the Fermi energy of the unperturbed system lies within the bulk band gap of the topological 2DEG, the action of the tip can therefore open or close underlying edge modes, depending on the sign of the tip voltage. If the effective tip size is comparable to the system length but smaller than the width, this will result in selective closing, or opening, of the edge or bulk modes over the entire device length. If the effective tip size is small compared to the device system length, it will not result in additional conduction channels for positive tip voltages, as the new channels will not extend from one end of the device to the other. However, closing of channels can still occur, if the tip size is larger than the spatial (lateral) extent of the edge channel. For very small tip sizes, the system will see the tip action as an impurity, which will interfere with open modes but will not cause the complete closing of channels.

In Fig. 6 we simulate the perturbation effect on the sample of the electric field created by the tip in the form of a Gaussian on-site energy potential [see Fig. 6(a)]. Taking into account the convention  $E = -eV$ , where  $-e$  is the electron charge, the positive (negative) on-site energies represent negative (positive) tip voltages applied in experiment. The Gaussian potential of the tip is characterized by two parameters, its maximum height  $V_0$  and its half width  $\sigma$ . If the tip is placed at position  $(x_0, y_0)$  above the device, the on-site potential function is written as

$$V(x, y) = V_0 \exp\left[-\frac{(x - x_0)^2 + (y - y_0)^2}{2\sigma^2}\right].$$

The full width at half maximum is then  $2\sqrt{2\ln(2)}\sigma \approx 2.4\sigma$  [Fig. 6(a)].

The numerical experiment is started by tuning the entire system so that its chemical potential lies within the gap, for example, at  $E = -3$  meV, as given by the red line in Fig. 3(a). The system can then be expected to have a conductance close to  $14e^2/h = (2 + 3 \times 4)e^2/h$ , as there are three doubly degenerate ME states running on each edge. Then a suitable local electric field for the tip is chosen, which after testing turns out to be several tens of meV. This is the maximum height of the Gaussian on-site energy we use for simulating the tip; the half-width is 50 nm for the simulations of Fig. 6. The simulated tip is applied at the halfway point of the length of the sample, at  $L/2$ , and is run from the edge, up to the middle of the bulk, while calculating the resulting two-terminal conductance. As a negative tip voltage suppresses states lying in the sample directly under it, conductance should decrease when the tip lies above open channels. Clearly (see Fig. 6), such channels lie at the edge, at in-gap energies. In Fig. 6 it can be seen that stronger tip potentials suppress more of the ME states. Also, even in a disordered system the features of edge state suppression should be readily observed.

On the other hand, the application of a positive voltage to the local probe in our simulations locally increases the Fermi energy level of the underlying electrons. However, for small tip sizes this will not open a complete channel conducting from the source on one side to the drain at the other side of the device. Therefore, one cannot expect any increase in conductance. In experiments with real samples the signatures of scattering induced in topological states due to charge puddles have been shown using this technique [41] for

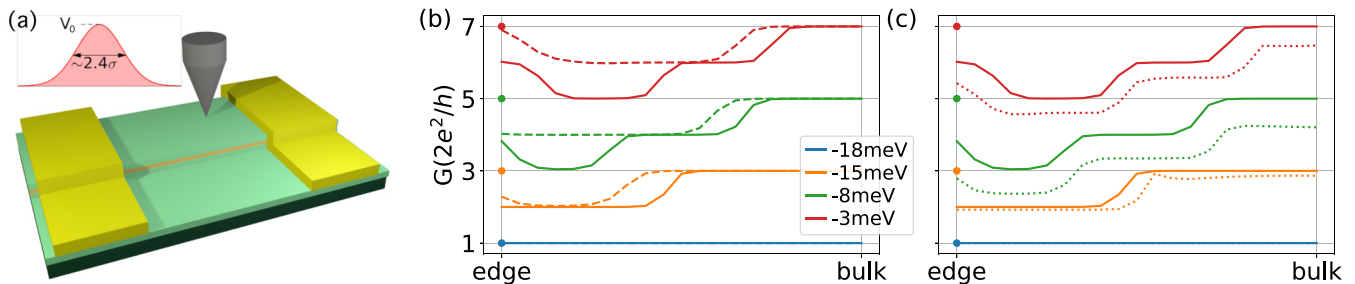


FIG. 6. (a) Cartoon of the experimental SGM setup. (b) Conductance results in a clean system at four different back gates [ $-18$  meV to  $-3$  meV, blue to red; see the corresponding horizontal cuts in Fig. 3(a)] and tip energies of  $10$  meV (dashed lines) and  $20$  meV (solid lines). (c) Same as (b) but for a  $20$  meV tip energy compared to results for a weakly disordered system (dotted lines).

devices with large stretches of edge. For shorter devices, we propose the selective tuning of states in a separate work [66].

An alternative experiment to infer the spatial distribution of states is the characterization of the spatial distribution of supercurrents flowing in a Josephson junction with a 2D TI material as the weak link. For HgTe quantum wells, in Ref. [67], a certain evolution of the spatial distribution of current as a function of applied gate voltage can be observed, which could correspond to the tuning of massive states, but could also correspond to other inhomogeneous electrostatic effects, or a combination of both.

### C. Selective tuning edge conductance via dedicated gate electrodes

In this section we propose an experimental design that allows one to selectively tune the contributions to conductance of ME states. On the one hand, in the case of systems with strong disorder this setup will reveal the presence of additional in-gap ME states and unequivocally distinguish their contribution to conductance from bulk percolation. On the other hand, and more interestingly, this setup allows one to isolate the contribution to conductance of the topological state from that of the ME extra states, which in most cases is undesired.

The setup is unsophisticated and technologically feasible, which makes its realization easily possible. One needs a 2D QW layer, with a back gate for sweeping the entire sample through the gap as well as a split top-gate electrode for the

edge and a top-gate electrode for the bulk, both running over the entire length [see Fig. 7(a)].

In our simulations we fixed the back gate so as to start from the top of the valence band, with a system containing only one topological state running at each lateral edge. Once this is fixed, one sweeps either the edge or the bulk gate through the energy range of the gap while measuring the two-terminal conductance.

In case there is anything more in the gap than just the topological state, one will find the conductance increasing in the gap while sweeping the edge gate. On the other hand, as there are no bulk states in the gap, the conductance should stay at (or close to) the  $2e^2/h$  value while sweeping the bulk gate. By subtracting one from the other, one can more precisely detect the difference. Even in systems with strong disorder, by subtracting bulk and edge gate sweeps, one can remove the disorder contribution to conductance.

This experimental setup would also allow for minimizing the effects of ME states. By applying edge gates to both lateral edges and tuning those suitably, one could dispose of a substantial number of the interface effects as described above.

### D. Quantum capacitance measurements

The capacitance of a device gives us information about how the electron density increases as we increase the electric potential applied to the system. It is the ratio of the electronic charge to the applied electric potential. In nanoscale systems,

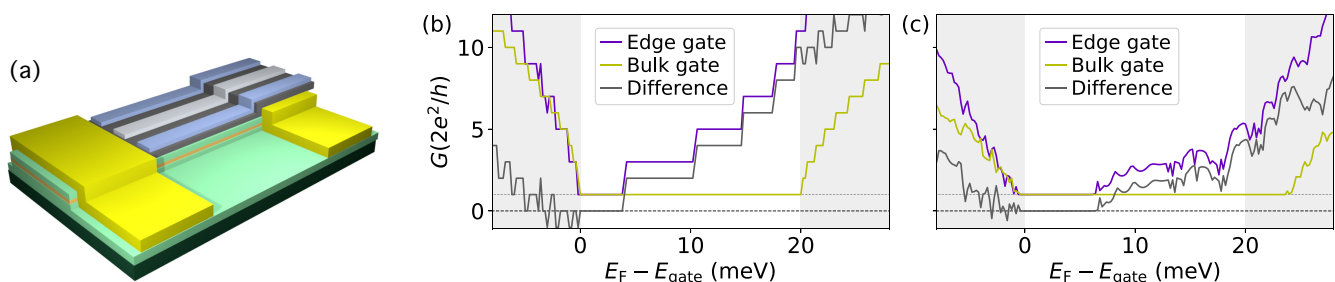


FIG. 7. (a) Experimental setup with local edge and bulk gates. (b) Conductance for a system with a local edge gate and a local bulk gate, when scanning through the local edge gate or the local bulk gate. The difference between these two measurements clearly shows there is more than the topological edge state in the gap. (c) Same as (b) but for a disordered system with  $U_0 = 100$  meV. In the presence of this disorder the gap is larger due to the negative renormalization of the gap parameter.



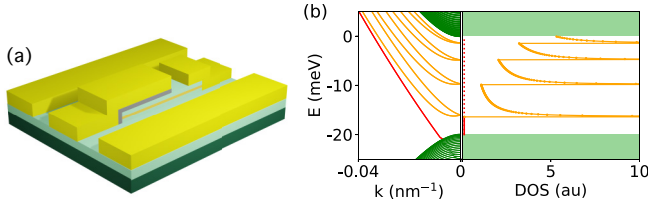


FIG. 8. (a) Possible experimental setup (see Ref. [73]). (b) In-gap density of states for a gap containing only topological bands (dashed red line) and for a gap containing topological bands (solid red line) and ME bands (dotted orange line).

besides the classical geometrical capacitance, there is also a contribution due to the quantum effects that become important at both small length scales and low temperature. The total capacitance is then given as

$$C_t^{-1} = C_g^{-1} + C_q^{-1}, \quad (7)$$

where  $C_g^{-1}$  is the geometrical capacitance and  $C_q^{-1}$  is the quantum capacitance. It can easily be shown that the quantum capacitance of a system is proportional to the density of states (DOS) around the electrochemical potential [68,69]. Measuring quantum capacitance is therefore a common tool in studying electronic properties in the topological phase [70–72]. Experimental evidence of VP states in 3D TI was observed in quantum capacitance experiments [45], and recent experimental reports in 2D HgTe QWs show values of the quantum capacitance exceeding the value due to the sole presence of topological edge states [73] [for a typical experimental setup see Fig. 8(a)]. In the case of a low-temperature system, we can write express the quantum capacitance as

$$C_q = -e^2 \int_{-\infty}^{+\infty} dE \rho(E) \left( \frac{\partial f}{\partial E} \right) = e^2 \rho(E_F + eV), \quad (8)$$

where  $\rho(E_F + eV)$  is the DOS at the Fermi energy shifted by an applied gate potential  $V$ . The total capacitance is thus dominated by the smallest of the geometrical or quantum capacitance. In the case of a gapped semiconductor the quantum capacitance in the gap is zero, as the in-gap density of states is zero. In topological materials, with an in-gap edge state, the DOS is constant but nonzero in the gap [see Fig. 8(b)].

For a system of length  $L$  the 1D contribution of the topological state to the DOS is given by

$$\rho_{\text{QSH}}(E) = \rho_{\text{QSH}} = \frac{2L}{\pi \hbar v_F}, \quad (9)$$

giving a quantum capacitance of  $C_q^0 = 0.19 \text{ nF m}^{-1}$  [74]. If there are in-gap ME states however, the DOS behaves very differently, having in-gap contributions of the ME states with paraboliclike dispersion. The DOS of these states is written as

$$\rho_{\text{ME}}(E) = L \sum_n \frac{\sqrt{2m^*}}{\pi \hbar} \frac{\Theta(E - E_n)}{\sqrt{E - E_n}}, \quad (10)$$

where  $m^*$  is the effective mass of the charge carriers and  $E_n$  is the onset energy of the  $n$ th massive band [75]. This gives a

quantum capacitance per unit length of

$$C_q = C_q^0 + \frac{e^2 \sqrt{2m^*}}{\pi \hbar} \sum_n \frac{\Theta(E - E_n)}{\sqrt{E - E_n}}, \quad (11)$$

implying that  $C_q > C_q^0$  in the presence of ME states. Here we are supposing the quantum contributions come only from (quasi)-1D edge states. In order to show that this is indeed the case, one could measure the capacitance of systems of different lengths [45,73,76]. Doing this type of measurement, one can separate the geometric capacitance contribution from the quantum capacitance. One can also do AC microwave capacitance spectroscopy that additionally gives access to the resistive response of the system, reflecting on the ability of the system to conduct. This resistive part should therefore additionally give information about how many states contribute to transport [77].

## V. CONCLUSION

In this work we have studied quantum wells hosting two-dimensional topological insulators within the Bernevig-Hughes-Zhang model. We have assumed that the mass and the on-site energy terms can vary smoothly at the interface between the bulk of the quantum well and the vacuum. We have shown the appearance of massive edge states in addition to the standard linearly dispersing mode of the quantum spin Hall effect. These massive edge states are characterized by a finite probability only close to the boundary of the system and by a spin-split paraboliclike energy dispersion. We have shown how these states can strongly affect the transport properties of a two-terminal system: The conductance of the system can increase above the nominal value of  $2e^2/h$  of the topological states. However, due to the parabolic energy dispersion, these massive edge states are susceptible to the effect of local disorder. We have proven that in the case of strong disorder, their effect on the transport properties can be completely eliminated. We have proposed various experimental setups that could pave the way for the detection and tunability of these massive edge states; these are mostly based on employing local probes and the design of local electrodes. Realistic samples are characterized by a more complex type of disorder as inhomogeneity and charge puddles. The latter can be included in our model, but their presence should not modify our findings substantially. Our results apply to the case of HgTe/CdTe and also to InAs/GaSb quantum wells; additionally, the general features we have shown should also be observable in two-dimensional materials presenting the quantum spin Hall effect such as silicene, bismuthene, and other van der Waals topological materials.

## ACKNOWLEDGMENTS

Discussions with E. Boquillon, A. De Martino, D. Goldhaber-Gordon, C. Gorini, S. Tchoumakov, and M. Wimmer are acknowledged. The work of T.L.v.d.B. and D.B. was supported by the Spanish Ministerio de Economía y Competitividad (MINECO) through Project No. FIS2014-55987-P, by Spanish Ministerio de Ciencia, Innovation y Universidades (MICINN) through Project No. FIS2017-82804-P, and by the Transnational Common Laboratory

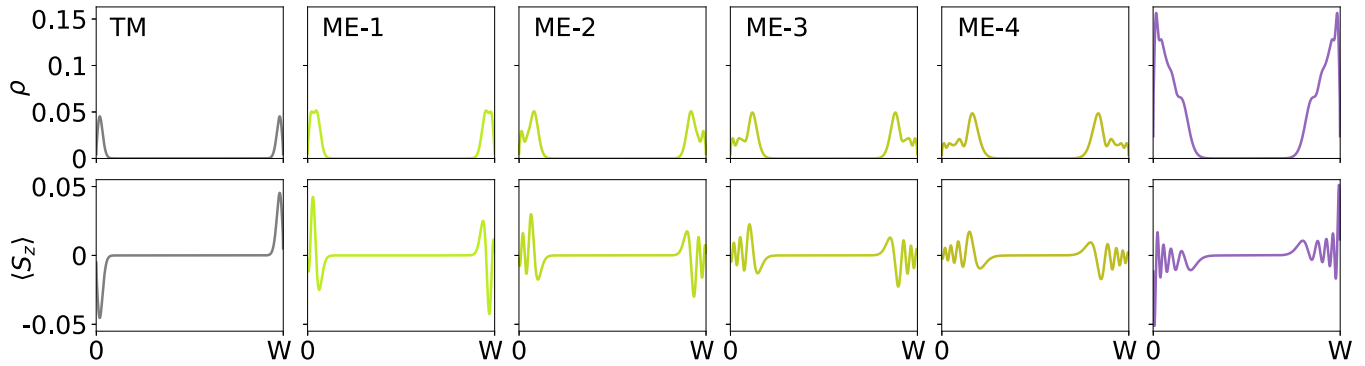


FIG. 9. Topological mode (left, gray), four different ME modes (middle, shades of green), and the sum of all available states at  $E = -1$  meV (right, purple), corresponding to the purple line in Fig. 3(a).

Quantum-ChemPhys. M.R.C. acknowledges funding from the Spanish Government through Project No. MAT2017-88377-C2-2-R (AEI/FEDER UE) and the Generalitat Valenciana through Grant No. Cidegnt2018004.

#### APPENDIX: A DEEPER LOOK INTO THE LOCAL DENSITY OF STATES

Here we will discuss how the different modes of the wave function add up to the local density of states. For each mode  $m$ , the wave function is the sum over all intersections  $k_x^i$  in the band structure at energy  $\varepsilon$ ,

$$\psi_m(y, \varepsilon) = \sum_i \psi_m[y, k_x^i(\varepsilon)], \quad (\text{A1})$$

where  $y$  gives the lateral dependence of the wave function. The local density of states is the square of the wave function, summed over all modes available at the Fermi energy,

$$\rho(y, \varepsilon) = \sum_m \rho_m(y, \varepsilon) = \sum_m |\psi_m(y, \varepsilon)|^2. \quad (\text{A2})$$

In a similar fashion, for the spin polarization we have

$$\begin{aligned} \langle \sigma_j \rangle(y, \varepsilon) &= \sum_m \langle \sigma_j(y, \varepsilon) \rangle_m \\ &= \sum_m \sum_i \psi_m^*[y, k_x^i(\varepsilon)] \sigma_j \psi_m[y, k_x^i(\varepsilon)]. \end{aligned} \quad (\text{A3})$$

As the ME states are two doubly degenerate spin-split modes, their spin components have both positive and negative values near each edge, resulting in local oscillations of each mode. Consecutive modes of higher energies move more and more into the bulk, resulting in more oscillations for higher-energy modes, as can be seen from Fig. 9. We also observe that for each consecutive mode, the main contribution to  $\rho(\varepsilon)$  moves farther away from the edge. This results in an overall oscillating  $\rho(\varepsilon)$ , with the number of oscillations depending on the number of ME modes available at energy  $\varepsilon$ .

- 
- [1] I. Tamm, *Phys. Z. Sowjetunion* **1**, 733 (1932).  
[2] W. Shockley, *Phys. Rev.* **56**, 317 (1939).  
[3] K. v. Klitzing, G. Dorda, and M. Pepper, *Phys. Rev. Lett.* **45**, 494 (1980).  
[4] R. B. Laughlin, *Phys. Rev. B* **23**, 5632 (1981).  
[5] B. I. Halperin, *Phys. Rev. B* **25**, 2185 (1982).  
[6] D. J. Thouless, M. Kohmoto, M. P. Nightingale, and M. den Nijs, *Phys. Rev. Lett.* **49**, 405 (1982).  
[7] D. B. Chklovskii, B. I. Shklovskii, and L. I. Glazman, *Phys. Rev. B* **46**, 4026 (1992).  
[8] K. Güven and R. R. Gerhardt, *Phys. Rev. B* **67**, 115327 (2003).  
[9] M. Z. Hasan and C. L. Kane, *Rev. Mod. Phys.* **82**, 3045 (2010).  
[10] X.-L. Qi and S.-C. Zhang, *Rev. Mod. Phys.* **83**, 1057 (2011).  
[11] C.-K. Chiu, J. C. Y. Teo, A. P. Schnyder, and S. Ryu, *Rev. Mod. Phys.* **88**, 035005 (2016).  
[12] F. D. M. Haldane, *Rev. Mod. Phys.* **89**, 040502 (2017).  
[13] C. L. Kane and E. J. Mele, *Phys. Rev. Lett.* **95**, 146802 (2005).  
[14] B. A. Bernevig and S.-C. Zhang, *Phys. Rev. Lett.* **96**, 106802 (2006).  
[15] B. A. Bernevig, T. L. Hughes, and S.-C. Zhang, *Science* **314**, 1757 (2006).  
[16] G. Gusev, Z. Kvon, E. Olshanetsky, and N. Mikhailov, *Solid State Commun.* **302**, 113701 (2019).  
[17] M. König, S. Wiedmann, C. Brüne, A. Roth, H. Buhmann, L. W. Molenkamp, X.-L. Qi, and S.-C. Zhang, *Science* **318**, 766 (2007).  
[18] A. Roth, C. Brüne, H. Buhmann, L. W. Molenkamp, J. Maciejko, X.-L. Qi, and S.-C. Zhang, *Science* **325**, 294 (2009).  
[19] C. Brüne, A. Roth, H. Buhmann, E. M. Hankiewicz, L. W. Molenkamp, J. Maciejko, X.-L. Qi, and S.-C. Zhang, *Nat. Phys.* **8**, 485 (2012).  
[20] K. C. Nowack, E. M. Spanton, M. Baenninger, M. König, J. R. Kirtley, B. Kalisky, C. Ames, P. Leubner, C. Brüne, H. Buhmann, L. W. Molenkamp, D. Goldhaber-Gordon, and K. A. Moler, *Nat. Mater.* **12**, 787 (2013).  
[21] E. Y. Ma, M. R. Calvo, J. Wang, B. Lian, M. Mühlbauer, C. Brüne, Y.-T. Cui, K. Lai, W. Kundhikanjana, Y. Yang, M. Baenninger, M. König, C. Ames, H. Buhmann, P. Leubner,

- L. W. Molenkamp, S.-C. Zhang, D. Goldhaber-Gordon, M. A. Kelly, and Z.-X. Shen, *Nat. Commun.* **6**, 7252 (2015).
- [22] M. R. Calvo, F. de Juan, R. Ilan, E. J. Fox, A. J. Bestwick, M. Mühlbauer, J. Wang, C. Ames, P. Leubner, C. Brüne, S. C. Zhang, H. Buhmann, L. W. Molenkamp, and D. Goldhaber-Gordon, *Phys. Rev. Lett.* **119**, 226401 (2017).
- [23] J. Strunz, J. Wiedenmann, C. Fleckenstein, L. Lunczer, W. Beugeling, V. L. Müller, P. Shekhar, N. T. Ziani, S. Shamim, J. Kleinlein, H. Buhmann, B. Trauzettel, and L. W. Molenkamp, *Nat. Phys.* **16**, 83 (2020).
- [24] C. Liu, T. L. Hughes, X.-L. Qi, K. Wang, and S.-C. Zhang, *Phys. Rev. Lett.* **100**, 236601 (2008).
- [25] I. Knez, R.-R. Du, and G. Sullivan, *Phys. Rev. Lett.* **107**, 136603 (2011).
- [26] K. Suzuki, Y. Harada, K. Onomitsu, and K. Muraki, *Phys. Rev. B* **87**, 235311 (2013).
- [27] T. Li, P. Wang, H. Fu, L. Du, K. A. Schreiber, X. Mu, X. Liu, G. Sullivan, G. A. Csáthy, X. Lin, and R.-R. Du, *Phys. Rev. Lett.* **115**, 136804 (2015).
- [28] Z. Fei, T. Palomaki, S. Wu, W. Zhao, X. Cai, B. Sun, P. Nguyen, J. Finney, X. Xu, and D. H. Cobden, *Nat. Phys.* **13**, 677 (2017).
- [29] S. Wu, V. Fatemi, Q. D. Gibson, K. Watanabe, T. Taniguchi, R. J. Cava, and P. Jarillo-Herrero, *Science* **359**, 76 (2018).
- [30] M. M. Ugeda, A. Pulkin, S. Tang, H. Ryu, Q. Wu, Y. Zhang, D. Wong, Z. Pedramrazi, A. Martín-Recio, Y. Chen, F. Wang, Z.-X. Shen, S.-K. Mo, O. V. Yazyev, and M. F. Crommie, *Nat. Commun.* **9**, 3401 (2018).
- [31] S. Tang, C. Zhang, D. Wong, Z. Pedramrazi, H.-Z. Tsai, C. Jia, B. Moritz, M. Claassen, H. Ryu, S. Kahn *et al.*, *Nat. Phys.* **13**, 683 (2017).
- [32] F. Yang, L. Miao, Z. F. Wang, M.-Y. Yao, F. Zhu, Y. R. Song, M.-X. Wang, J.-P. Xu, A. V. Fedorov, Z. Sun, G. B. Zhang, C. Liu, F. Liu, D. Qian, C. L. Gao, and J.-F. Jia, *Phys. Rev. Lett.* **109**, 016801 (2012).
- [33] F. Reis, G. Li, L. Dudy, M. Bauernfeind, S. Glass, W. Hanke, R. Thomale, J. Schäfer, and R. Claessen, *Science* **357**, 287 (2017).
- [34] I. K. Drozdov, A. Alexandradinata, S. Jeon, S. Nadj-Perge, H. Ji, R. J. Cava, B. A. Bernevig, and A. Yazdani, *Nat. Phys.* **10**, 664 (2014).
- [35] K. Kandrai, G. Kukucska, P. Vancsó, J. Koltai, G. Baranka, Z. E. Horváth, A. Hoffmann, A. Vymazalová, L. Tapasztó, and P. Nemes-Incze, Evidence for room temperature quantum spin Hall state in the layered mineral jacutingaite, [arXiv:1903.02458](https://arxiv.org/abs/1903.02458).
- [36] J. Maciejko, C. Liu, Y. Oreg, X.-L. Qi, C. Wu, and S.-C. Zhang, *Phys. Rev. Lett.* **102**, 256803 (2009).
- [37] A. Ström, H. Johannesson, and G. I. Japaridze, *Phys. Rev. Lett.* **104**, 256804 (2010).
- [38] F. Crépin, J. C. Budich, F. Dolcini, P. Recher, and B. Trauzettel, *Phys. Rev. B* **86**, 121106(R) (2012).
- [39] T. L. Schmidt, S. Rachel, F. von Oppen, and L. I. Glazman, *Phys. Rev. Lett.* **108**, 156402 (2012).
- [40] J. I. Väyrynen, M. Goldstein, and L. I. Glazman, *Phys. Rev. Lett.* **110**, 216402 (2013).
- [41] M. König, M. Baenninger, A. G. F. Garcia, N. Harjee, B. L. Pruitt, C. Ames, P. Leubner, C. Brüne, H. Buhmann, L. W. Molenkamp, and D. Goldhaber-Gordon, *Phys. Rev. X* **3**, 021003 (2013).
- [42] S. Essert, V. Krueckl, and K. Richter, *Phys. Rev. B* **92**, 205306 (2015).
- [43] B. A. Volkov and O. A. Pankratov, *JETP Lett.* **42**, 178 (1985).
- [44] O. A. Pankratov, *Phys. Usp.* **61**, 1116 (2018).
- [45] A. Inhofer, S. Tchoumakov, B. A. Assaf, G. Fève, J. M. Berroir, V. Jouffrey, D. Carpentier, M. O. Goerbig, B. Plaçais, K. Bendias, D. M. Mahler, E. Bocquillon, R. Schlereth, C. Brüne, H. Buhmann, and L. W. Molenkamp, *Phys. Rev. B* **96**, 195104 (2017).
- [46] S. Tchoumakov, V. Jouffrey, A. Inhofer, E. Bocquillon, B. Plaçais, D. Carpentier, and M. O. Goerbig, *Phys. Rev. B* **96**, 201302(R) (2017).
- [47] D. M. Mahler, J.-B. Mayer, P. Leubner, L. Lunczer, D. Di Sante, G. Sangiovanni, R. Thomale, E. M. Hankiewicz, H. Buhmann, C. Gould, and L. W. Molenkamp, *Phys. Rev. X* **9**, 031034 (2019).
- [48] M. Seo, C. Hong, S.-Y. Lee, H. K. Choi, N. Kim, Y. Chung, V. Umansky, and D. Mahalu, *Sci. Rep.* **4**, 3806 (2014).
- [49] W. Mönch, in *Semiconductor Surfaces and Interfaces*, 3rd ed., edited by G. Ertl, R. Gomer, H. Lüth, and D. L. Mills (Springer, Berlin, 2001).
- [50] R. Skolasinski, D. I. Pikulin, J. Alicea, and M. Wimmer, *Phys. Rev. B* **98**, 201404(R) (2018).
- [51] M. König, H. Buhmann, L. W. Molenkamp, T. Hughes, C.-X. Liu, X.-L. Qi, and S.-C. Zhang, *J. Phys. Soc. Jpn.* **77**, 031007 (2008).
- [52] K. Ortner, X. C. Zhang, A. Pfeuffer-Jeschke, C. R. Becker, G. Landwehr, and L. W. Molenkamp, *Phys. Rev. B* **66**, 075322 (2002).
- [53] C. W. Groth, M. Wimmer, A. R. Akhmerov, and X. Waintal, *New J. Phys.* **16**, 063065 (2014).
- [54] M. Governale and U. Zülicke, *Phys. Rev. B* **66**, 073311 (2002).
- [55] C. A. Perroni, D. Bercioux, V. M. Ramaglia, and V. Cataudella, *J. Phys.: Condens. Matter* **19**, 186227 (2007).
- [56] S. Smirnov, D. Bercioux, and M. Grifoni, *Europhys. Lett.* **80**, 27003 (2007).
- [57] D. Bercioux and P. Lucignano, *Rep. Prog. Phys.* **78**, 106001 (2015).
- [58] D. G. Rothe, R. W. Reinthaler, C.-X. Liu, L. W. Molenkamp, S.-C. Zhang, and E. M. Hankiewicz, *New J. Phys.* **12**, 065012 (2010).
- [59] H. Jiang, L. Wang, Q.-f. Sun, and X. C. Xie, *Phys. Rev. B* **80**, 165316 (2009).
- [60] C. W. Groth, M. Wimmer, A. R. Akhmerov, J. Tworzydło, and C. W. J. Beenakker, *Phys. Rev. Lett.* **103**, 196805 (2009).
- [61] B. Wu, J. Song, J. Zhou, and H. Jiang, *Chin. Phys. B* **25**, 117311 (2016).
- [62] J. A. Stroscio and R. M. Feenstra, in *Scanning Tunneling Microscopy*, edited by J. A. Stroscio and W. J. Kaiser (Academic, San Diego, 1993), Vol. 27.
- [63] H. Söde, L. Talirz, O. Gröning, C. A. Pignedoli, R. Berger, X. Feng, K. Müllen, R. Fasel, and P. Ruffieux, *Phys. Rev. B* **91**, 045429 (2015).
- [64] G. Buchs, D. Bercioux, L. Mayrhofer, and O. Gröning, *Carbon* **132**, 304 (2018).
- [65] N. Avraham, J. Reiner, A. Kumar-Nayak, N. Morali, R. Batabyal, B. Yan, and H. Beidenkopf, *Adv. Mater.* **30**, 1707628 (2018).
- [66] M. R. Calvo *et al.* (unpublished).
- [67] S. Hart, H. Ren, T. Wagner, P. Leubner, M. Mühlbauer, C. Brüne, H. Buhmann, L. W. Molenkamp, and A. Yacoby, *Nat. Phys.* **10**, 638 (2014).

- [68] S. Luryi, *Appl. Phys. Lett.* **52**, 501 (1988).
- [69] S. Datta, *Quantum Transport—Atom to Transistor* (Cambridge University Press, Cambridge, 2005).
- [70] D. A. Kozlov, M. L. Savchenko, J. Ziegler, Z. D. Kvon, N. N. Mikhailov, S. A. Dvoretiskii, and D. Weiss, *JETP Lett.* **104**, 859 (2016).
- [71] T. Kernreiter, M. Governale, and U. Zülicke, *Phys. Rev. B* **93**, 241304(R) (2016).
- [72] L. S. Braginsky and M. V. Entin, *Phys. Status Solidi B* **256**, 1800675 (2019).
- [73] M. C. Dartiailh, S. Hartinger, A. Gourmelon, K. Bendias, H. Bartolomei, H. Kamata, J.-M. Berroir, G. Fève, B. Plaçais, L. Lunczer, R. Schlereth, H. Buhmann, L. W. Molenkamp, and E. Bocquillon, Dynamical separation of bulk and edge transport in HgTe-based 2D topological insulators, [arXiv:1903.12391](https://arxiv.org/abs/1903.12391).
- [74] M. V. Entin and L. Braginsky, *Phys. Rev. B* **96**, 115403 (2017).
- [75] G. Grosso and G. Parravicini, *Solid State Physics* (Elsevier, Oxford, 2000).
- [76] T. Fang, A. Konar, H. Xing, and D. Jena, *Appl. Phys. Lett.* **91**, 092109 (2007).
- [77] E. Pallecchi, A. C. Betz, J. Chaste, G. Fève, B. Huard, T. Kontos, J.-M. Berroir, and B. Plaçais, *Phys. Rev. B* **83**, 125408 (2011).